JOURNAL OF MATERIALS SCIENCE 41 (2006) 77–86

Voltage tunable epitaxial $Pb_xSr_{(1-x)}TiO_3$ films on sapphire by MOCVD: Nanostructure and microwave properties

S.K. DEY*, C.G. WANG, W. CAO, S. BHASKAR, J. LI
Department of Chemical and Materials Engineering & Electrical Engineering, Ira A. Fulton School of Engineering, Arizona State University, Tempe, AZ 85287-6006, USA
E-mail: Sandwip.dey@asu.edu

G. SUBRAMANYAM
Department of Electrical and Computer Engineering, University of Dayton, Dayton, OH 45469-0226, USA

Frequency and phase agile microwave components such as tunable filters and phase shifters will require ferroelectric thin films that exhibit a nonlinear dependence of dielectric permittivity (ε_r) with dc electric bias, as well as a high material ($\Delta\varepsilon_r$/tan δ) and device (or K-factor in phase shift/dB) figure of merits (FOM). Therefore, voltage tunable $(Pb_{0.3}Sr_{0.7})TiO_3$ (PST) thin films (90–150 nm) on (0001) sapphire were deposited by metal-organic chemical vapor deposition at rates of 10–15 nm/min. The as-deposited epitaxial PST films were characterized by Rutherford backscattering spectroscopy, X-ray methods, field emission scanning electron microscope, high resolution transmission electron microscopy, Raman spectroscopy, and electrical methods (7–17 GHz) using coplanar waveguide test structures. The epitaxial relationships were as follows: out-of-plane alignment of [111] PST//[0001] sapphire, and orthogonal in-plane alignments of $[1\bar{1}0]$ PST//$[10\bar{1}0]$ sapphire and $[\bar{1}\bar{1}2]$ PST//$[1\bar{2}10]$ sapphire. The material FOM and device FOM (or K-factor) at 12 GHz were determined to be 632 and ~13 degrees/dB, respectively. The results are discussed in light of the nanostructure and stress in epi-PST films. Finally, a rational basis for the selection of PST composition, substrate, and process parameters is provided for the fabrication of optimized coplanar waveguide (CPW) phase shifters with very high material and device FOMs. © *2006 Springer Science + Business Media, Inc.*

1. Introduction

Perovskite materials (e.g., $SrTiO_3$ and $Ba_xSr_{(1-x)}TiO_3$) with voltage tunable dielectric behavior (i.e., percent change in dielectric permittivity, ε_r, with dc bias) have been used for components such as phase-shifters (in phased-array antennas for radar) and preselect filters (in receivers for communication and radar) [1, 2]. Such applications require high ε_r for reducing device size, large dielectric tunability for frequency and phase agility, fast polarization response, and low dielectric loss tangent (or high Q) at microwave frequencies [3]. Frequency and phase agile microwave components such as tunable resonators, filters, local oscillators, and phase shifters have been already demonstrated at Ku- and K-band frequencies using ferroelectric thin films and microstrip transmission lines [4–6]. Although microstrip circuits are the most common transmission line component for microwave frequencies, when used in monolithic microwave integrated circuits (MMICs), the ground-plane is difficult to access for shunt connections necessary for active devices. Therefore, a coplanar waveguide (CPW) design is attractive since the ground conductor runs adjacent to the conductor strip, and the ease of monolithic integration. Findikoglu *et al.* demonstrated a tunable filter in CPW configuration with large tunability (>15%), and the electrical tuning resulted in improved filter characteristics [7]. Wilbur *et al.*

*Author to whom all correspondence should be addressed.

0022-2461 © *2006 Springer Science + Business Media, Inc.*
DOI: 10.1007/s10853-005-5926-4

[8] studied CPW-based phase shifter circuits in which the frequency and phase agility was achieved through the use of ferroelectric thin films that exhibit a nonlinear dependence of ε_r with dc electric bias. The material figure of merit (FOM), used for tunable microwave phase shifters, is an electrical parameter, which is directly proportional to the tunability and inversely proportional to the loss tangent (tan δ), whereas, the device FOM is characterized by the K-factor (phase shift/dB).

From a materials standpoint, $SrTiO_3$ has to be used at low temperatures, due to its lower incipient Curie transition temperature, T_c, and its structural compatibility with high temperature superconductor thin films. Therefore, to date, $Ba_xSr_{(1-x)}TiO_3$ or BST has been the most widely studied ferroelectric thin-film system for room-temperature microwave applications. However, due to the relatively high tan δ and difficulty in processing stoichiometric BST films, the search of alternative materials has been warranted. Recently, an alternative perovskite material system, $Pb_xSr_{(1-x)}TiO_3$ (or PST), has been explored for potential microwave applications at room temperature [9]. In this PST system, the T_c may be readily controlled by changing x; for $x \sim 0.3$, the $T_c \sim 20°C$ and room temperature operation can be in the Curie-Weiss region. Due to the disappearance of ferroelectric hysteresis at room temperature, bulk $(Pb_{0.3}Sr_{0.7})TiO_3$ is expected to show low dielectric loss in its paraelectric state. Indeed, the low frequency (1 MHz) tan δ and tunability for bulk PST (30/70) were measured to be <0.001 and 70%, respectively [9]. From a structure-property viewpoint, an understanding of the origin and subsequent engineering of the stress or strain is also important since previous studies have reported a strong correlation between the strain and microwave dielectric properties in BST films [10, 11]. In one such study, films deposited in oxygen pressures, varying from 2–100 mTorr, exhibited a range (0.996–1.003) in degree of tetragonal distortion, D (D = ratio of the in-plane to out-of-plane lattice parameters). Interestingly, at microwave frequencies (1–20 GHz), films with the highest material FOM of ~800 were observed in films that had the minimum strain or D = 1 [10].

In this current work, a reproducible metal-organic chemical vapor deposition (MOCVD) process for the deposition of epitaxial PST thin films (at high deposition rates) on sapphire (hexagonal Wurtzite structure) is demonstrated by using a direct liquid injection (DLI) system. Since sapphire has low ε_r (9.4 for c-cut) and tan δ (0.0003 for c-cut), and is available at a reasonable price, it was a substrate of choice. The PST films were first characterized by various techniques (RBS, XRD, FESEM, Raman, and HRTEM) to determine the composition and nanostructure. Next, CPW test structures (i.e., transmission line and resonator structures typical for microwave devices) were fabricated to evaluate the tunability, loss, and material and device FOMs between 7 to 17 GHz. Specifically, the conductor and dielectric losses were extracted using quasi-static conformal mapping techniques [12, 13]. Here, the ε_r, tunability, and tan δ are discussed in light of the nanostructure and stress in epi-PST films on sapphire. Finally, a rational basis for the selection of PST composition, substrate, and process parameters is provided for the fabrication of optimized CPW phase shifters with very high material and device FOMs.

TABLE I MOCVD process parameters for $Pb_xSr_{(1-x)}TiO_3$ thin films on sapphire

Precursors/solvent	0.1 M $Pb(thd)_2$ in C_4H_8O (THF) 0.1 M $Sr(thd)_2$ in C_4H_8O 0.3 M $Ti(^tOBu)_2(thd)_2$ in C_4H_8O thd = $O_2C_{11}H_{19}$; ^tBu = tert-C_4H_9
Deposition parameters	
Shimadzu DLI flow rate (Pb, Sr, Ti)	0.1–0.2, 0.1–0.3, 0.5–0.7 cc/min
Carrier gas (Ar) flow rate	300 sccm
Oxygen flow rate	1000–2000 sccm
Vaporizer temperature	250°C
Vaporizer pressure	3–8 Torr
Reactor pressure	~1 Torr
Substrate temperature	500–700°C
Deposition rates	10–15 nm/min

2. Experimental

2.1. Processing of epitaxial $Pb_xSr_{(1-x)}TiO_3$ films on sapphire by MOCVD

The precursors and MOCVD processing parameters are tabulated in Table I. For the deposition of epi-$Pb_xSr_{(1-x)}TiO_3$ thin films (90–150 nm) on 2-inch (0001) sapphire (Saint-Gobain Crystals & Detectors), $Pb(thd)_2$, $Ti(^tOBu)_2(thd)_2$, and $Sr(thd)_2$, dissolved in THF solvent and contained in three metal containers, were used as the liquid precursors. A Shimadzu direct liquid injection (DLI) system was used to deliver these precursors, at controlled flow rates, to a mixer and then into a vaporizer. A high purity Ar carrier-gas delivered the vaporized precursors into the reactor via a showerhead, while a separate line was used to introduce oxygen for reaction with the precursors near the substrate surface.

2.2. RBS, FESEM, Raman

The Rutherford backscattering spectroscopy (RBS) was performed for composition analysis using a 1.7 MV Tandetron Accelerator (General Ionex Corp.). The morphology of the films was analyzed using a Hitachi S4700 field emission scanning electron microscope (FESEM). For the Raman spectra of PST and $PbTiO_3$ films, the 514.5 nm line of an Ar^+ laser (2020, Spectra-Physics, Mountain View, CA) was used. The laser beam was focused onto the sample surface, using a 50X objective (Mitutoyo, Japan), to a spot size of ~3–4 μm. The spectra were recorded using a single-stage monochromator

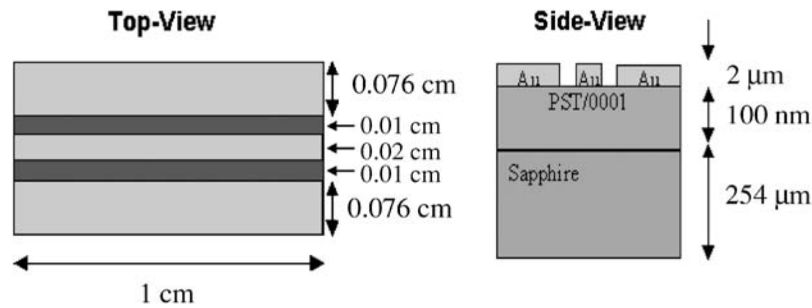

Figure 1 Coplanar waveguide (CPW) transmission line to determine the K-factor or figure of merit as phase shift/dB loss.

(HR640, ISA Instruments, Cedex, France) with a liquid-nitrogen-cooled CCD detector, and a filter (SuperNotch, Kaiser Optical Systems, Inc., Ann Arbor, MI) to eliminate plasma lines.

2.3. XRD, pole figure, and HRTEM

A Rigaku D/Max-IIB diffractometer was used for various X-ray diffraction (XRD) techniques to characterize the crystallinity and texture of the samples. A typical θ–2θ plot was generated to determine the composition, structure, and out-of-plane texture. The pole figures were obtained using the Rigaku pole figure attachment on a rotating anode generator. The data was recorded in reflection mode, with both alpha (15°–89°) and beta (0°–360°) steps of 2 degrees and collection time of 1 s at each step. For determination of nanostructure and for corroboration with X-ray analyses, high-resolution transmission electron microscopy (HRTEM; JEOL 4000EX, Japan) was also carried out on cross sectional samples. The relative in-plane and out-of-plane orientations between the PST film and sapphire substrate were determined by indexing the optical diffractograms obtained from HRTEM images. In order to confirm whether the PST film was under any in-plane stress, an off-axis X-ray scan was carried out. In this method, the effect of in-plane stress on the magnitude of the interplanar spacing of planes parallel (or inclined at angles $<45°$) to the film surface is determined. To accomplish this, the PST film was tilted so that the (110) planes of PST were perpendicular to the X-ray source-detector plane.

2.4. High frequency measurements

In the current approach, tunable CPW components were designed using the modified dielectric/ferroelectric/conductor configuration, and fabricated. The geometric layout consisted of a dielectric substrate (254 μm thick sapphire), a PST ferroelectric thin-film layer (100 nm thick), a 2 μm gold thin-film for the conductor (center line) and ground lines (adjacent parallel lines). The test structures, used to determine the material and device FOMs, included a CPW transmission line

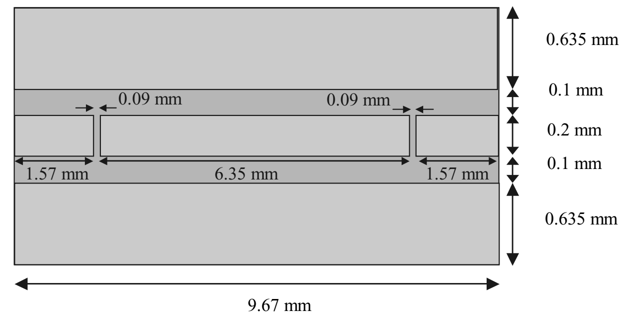

Figure 2 Transmission type resonator to determine the loss tangent of PST thin film.

and a CPW resonator. The transmission lines (Fig. 1) were designed for 0.6 cm, and 1 cm length with a center conductor width of 0.02 cm, and a gap between center conductor and the ground line of 0.01 cm. The resonator (Fig. 2) was a transmission type resonator coupled to input and output feed lines. It was primarily used to determine the tan δ of the PST film. The CPW line and resonator electrode structures were deposited on the samples in an electron beam evaporation system using shadow masks. The exposed (open) areas of the shadow mask defined the electrode structures on the samples, and after Au electrode deposition, the samples were annealed at 550°C for approximately 30 min in flowing nitrogen.

The high frequency measurements were performed inside a closed cycle cryogenic system modified for on-wafer CPW measurements. A HP 8510C automatic network analyzer was used for swept frequency microwave measurements. The dc bias voltage to the signal conductor was applied using a high voltage bias tee. A Thru-Reflect-Load (TRL) calibration was performed before the actual measurements.

As a preliminary check for tunability and magnitude of tan δ for PST film, the frequency dependence of the insertion loss (magnitude of S_{21}) was plotted for applied dc bias of 0 V bias and 400 V between the center conductor and the ground lines. The phase of S_{21} (plotted as total phase angle versus frequency) was compared at a specific frequency to determine the phase shift between zero bias and 400 V bias. Note, a large phase shift corresponds to a high tunability of the sample.

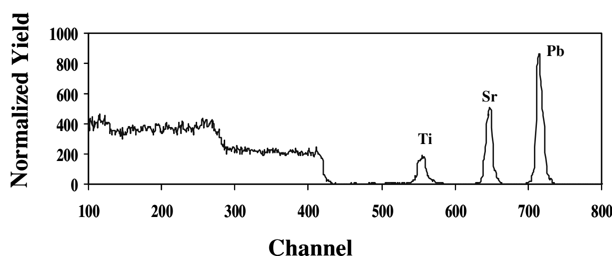

Figure 3 RBS of 100 nm $(Pb_{0.3}Sr_{0.7})TiO_3$ film on (0001) sapphire.

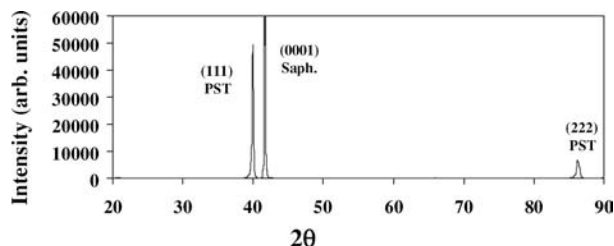

Figure 4 A θ–2θ XRD scan for 100 nm $(Pb_{0.3}Sr_{0.7})TiO_3$ film on (0001) sapphire.

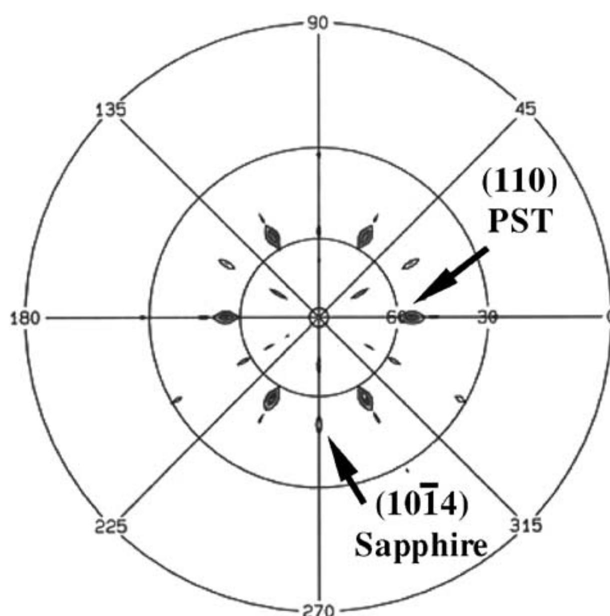

Figure 5 (110) Pole figure of (111) oriented $(Pb_{0.5}Sr_{0.7})TiO_3$ film (100 nm thick) on (0001) sapphire.

The swept frequency S-parameters were used to extract the ε_r (V) of the PST film by using the conformal mapping techniques [12, 13]. Also, from the resonance peak of the CPW resonator, the loaded Quality factor (i.e., Q_L = center frequency/3dB bandwidth) was determined, from which the unloaded Quality factor (Q_u) was calculated ($Q_u = Q_L \times S_{21}/(1-S_{21})$ and tan δ of the PST film is approximately $1/Q_u$). From the S-parameter measurements, the material FOM and the device FOM (i.e., K-factor in phase shift/dB) were determined. Please note that for calculation of the latter, the worst-case insertion loss was used. Once the ε_r and the tan δ of PST were obtained, the dielectric and conductor losses (in units of dB/cm) in the CPW line were extracted using a quasi-static TEM approximation of the CPW line, and conformal mapping techniques [12, 13].

3. Results and discussion

3.1. RBS, XRD, and pole figure

Fig. 3 shows the RBS spectrum of a 100 nm PST film deposited at 700°C by MOCVD on sapphire. The calculated composition of the PST film from a RUMP simulation was $(Pb_{0.3}Sr_{0.7})TiO_3$. The carbon contamination in the film was below the detection limit (0.5 atomic %). The XRD θ–2θ scan of the same film is shown in Fig. 4. Three major peaks in the regular spectrum are indexed as (111) PST, (0001) sapphire, and (222) PST. The high intensity of (111) PST peak indicates the general out-of-plane alignment in the [111] PST direction. The (110) pole figure, illustrated in Fig. 5, was carried out to demonstrate the high in-plane orientation of the film. The {110} PST poles with 6-fold symmetry were identified from the angular relationship (~35°) between the diffraction spots and the (111) plane. Also, the {10$\bar{1}$4} poles of sapphire with 3-fold symmetry are depicted in the same plot. The sharp contours of {110} poles of PST and {10$\bar{1}$4} poles of sapphire, along with their narrow intensity distribution, indicates clearly that PST grows epitaxially on sapphire. It is noted that all other low-density spots are related to the imperfection of the sapphire single crystal, which were verified by a pole figure (not shown here) obtained from a bare sapphire substrate under the same condition.

3.2. FESEM, HRTEM, Raman spectroscopy and origin of stress

A cross sectional FESEM image of a PST (150 nm)/sapphire interface is shown in Fig. 6. The PST film is dense and exhibits a single crystal like cleavage. A TEM image at low magnification (Fig. 7) shows threading dislocations; the number density of such dislocations which stem from the sapphire substrate was estimated to be $\sim 10^{10}$ cm^{-2}.

Fig. 8 illustrates a cross-sectional HRTEM image of the PST/sapphire interface, and optical diffractograms from regions within PST and sapphire. The observed interplanar spacing of sapphire: d_{006}(Sapphire) = 2.165 Å, d_{104}(Sapphire) = 2.551 Å, $d_{\bar{1}02}$(Sapphire) = 3.479 Å, and d_{300}(Sapphire) = 1.374 Åare as expected, whereas of PST: d_{110}(PST) = 2.780 Å, d_{111}(PST) = 2.276 Å, and d_{201}(PST) = 1.778 Åare consistently larger with respect to the bulk values [14]; similar observations for BST films on MgO substrate, in which the lattice parameters of the film were larger than their bulk values, have been

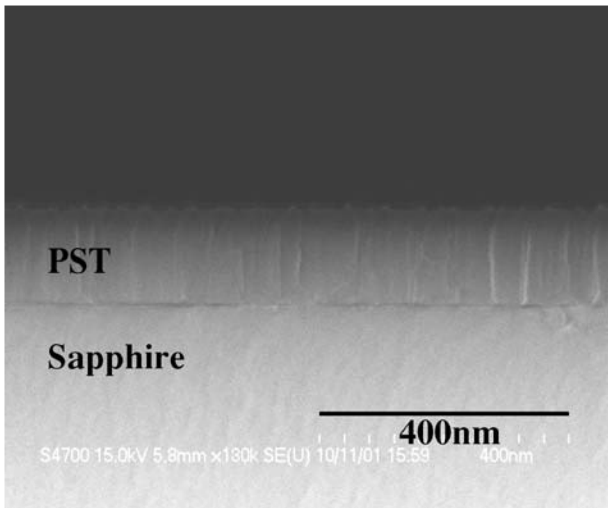

Figure 6 FESEM of $(Pb_{0.3}Sr_{0.7})TiO_3$ film on (0001) sapphire by MOCVD.

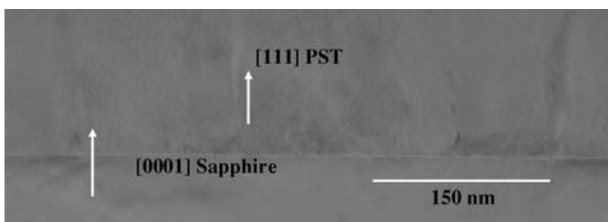

Figure 7 A low magnification TEM image showing defects in $(Pb_{0.3}Sr_{0.7})TiO_3$ film on sapphire.

reported elsewhere [15]. However, the as-deposited PST film is epitaxial and the orientation relationships, determined from the analyses of the diffractograms as well as all interplanar spacing, were as follows: out-of-plane alignment of [111] PST // [0001] sapphire, and orthogonal in-plane alignments of $[1\bar{1}0]$ PST//$[10\bar{1}0]$ sapphire and $[\bar{1}\bar{1}2]$ PST//$[1\bar{2}10]$ sapphire. Based on the HRTEM analyses, the in-plane atomic arrangements on (0001) sapphire and (111) PST planes, the overall orientation relationship of PST with respect to sapphire may be represented by the schematics of Fig. 9a and b, respectively; results which are consistent with the orientational relationships of PLZT on sapphire [16].

The observation of epitaxy in this large lattice-mismatched system (e.g., $d_{10\bar{1}0}$(sapphire) = 4.122 Åand $d_{1\bar{1}0}$(PST) = 2.780 Å) may be characterized by geometric epitaxy or domain matched epitaxy [17], i.e., although the misfit, f_1 (where, $f_1 = [d_{10\bar{1}0}\text{-}d_{1\bar{1}0}] \times 2/[d_{10\bar{1}0} + d_{1\bar{1}0}]$), is apparently large (38.9%), three interplanar spacing of $(1\bar{1}0)$ PST closely match with two interplanar spacing of $(10\bar{1}0)$ sapphire. This geometric matching gives a residual domain misfit, f_d (where, $f_d = [3d_{1\bar{1}0} - 2d_{10\bar{1}0}] \times 2/[3d_{1\bar{1}0} + 2d_{10\bar{1}0}]$), of only 1.16%, but the PST film in this direction still remains under compression. Similarly, the PST is also under a compressive stress in the orthogonal in-plane $[\bar{1}\bar{1}2]$ direction through geometric epitaxy; which means that if there exists bi-axial (in-plane) compressive stress, the out-of-plane [111] PST direction should be under tension [18]. Indeed, an off-axis (110) θ–2θ scan (Fig. 10) clearly shows a 0.49% extension or strain of the (110) lattice spacing of PST, which is also indicative of a residual tensile stress in the [111] PST direction.

Fig. 11 illustrates a Raman spectrum of 100 nm PST film on (0001) sapphire. For comparison, the Raman spectrum of iso-structural $PbTiO_3$ film (420 nm thick) is shown in the same figure. The sharp peaks at 417 cm^{-1},

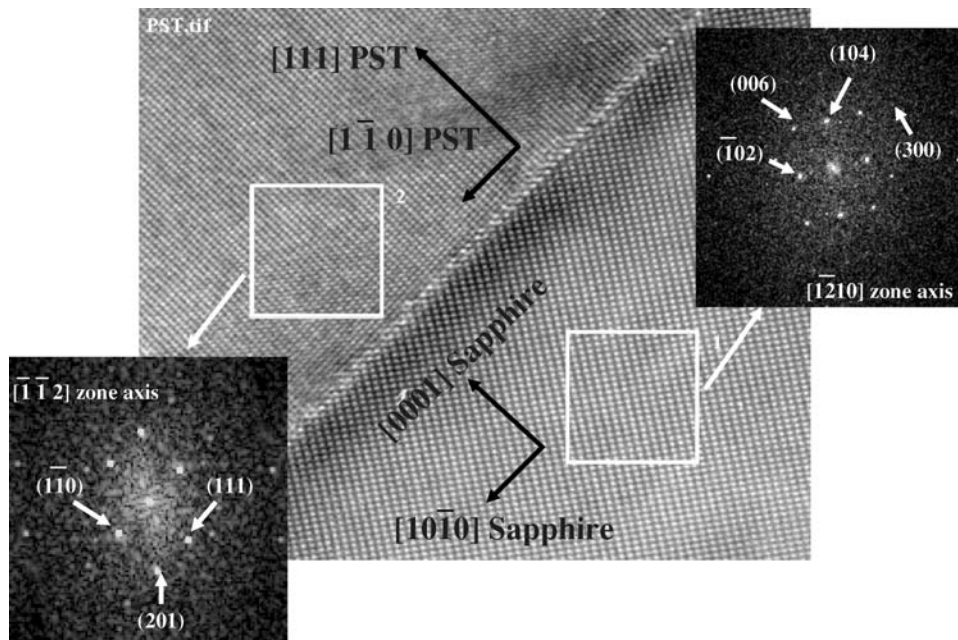

Figure 8 HRTEM of $(Pb_{0.3}Sr_{0.7})TiO_3$ film by MOCVD and optical diffractograms from regions within PST and sapphire.

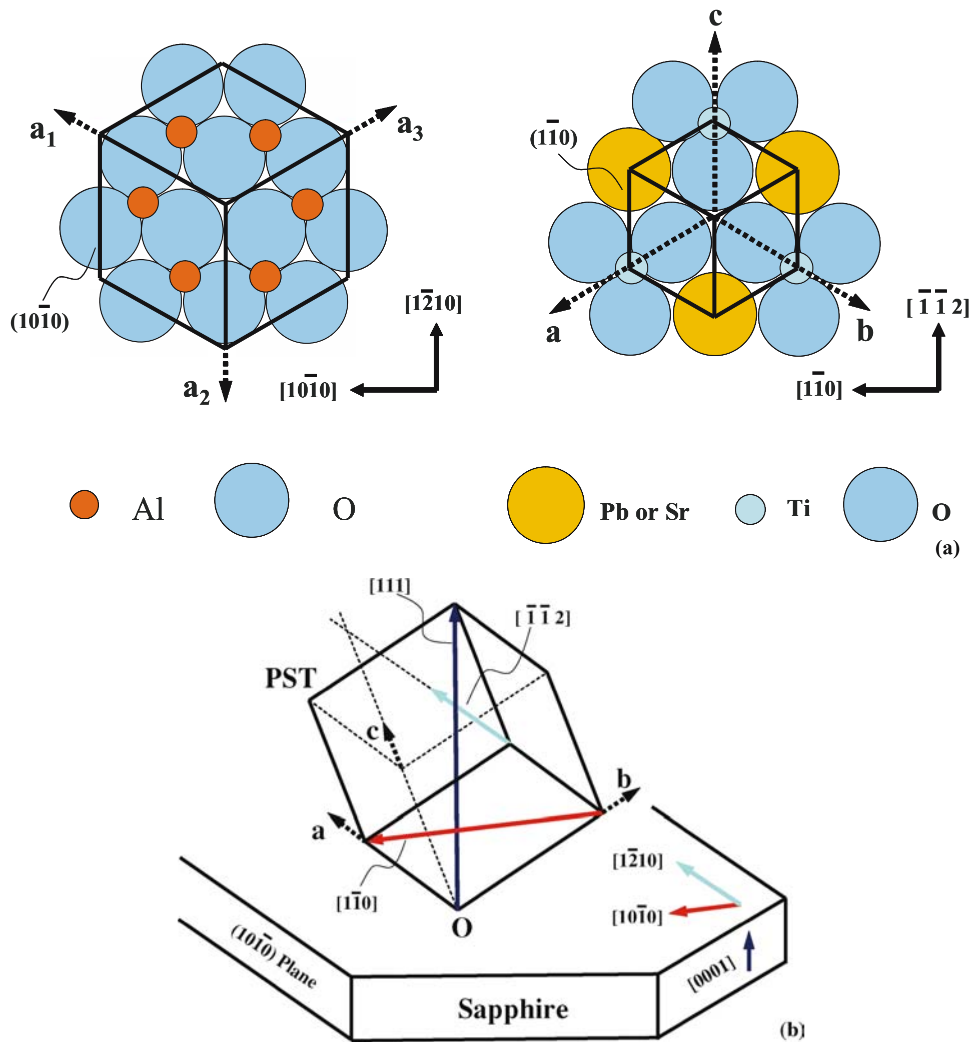

Figure 9 (a) Planar atomic configurations for sapphire basal plane and (111) PST plane; (b) Schematic of the orientation relationships for epitaxial PST on (0001) sapphire.

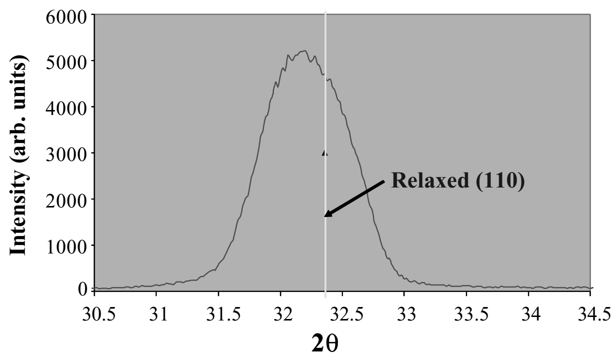

Figure 10 An off-axis $\theta-2\theta$ scan for the (110) PST plane. Here, d_{110} (0.278 nm, $2\theta = 32.2°$) of PST film is greater than d_{110} (0.2766 nm, $2\theta = 32.36°$) of relaxed or bulk PST.

578 cm^{-1}, and 752 cm^{-1} are assigned to sapphire, and the PST spectrum has been cut out in the low frequency region (<100 cm^{-1}, where the "soft mode" exists in $PbTiO_3$ system) due to artifacts from the measurement system. The PST spectrum indicates that the incorporation of Sr into the $PbTiO_3$ lattice results in a structural disorder, and the difference between the wavenumbers for the E(TO) and A1(TO) modes are closer compared to the $PbTiO_3$ spectrum. These are indicative of lattice transformation from tetragonal ferroelectric (in pure $PbTiO_3$) to the cubic paraelectric state (in PST); as found in a previous study E(TO) and A1(TO) modes, these phonons are indistinguishable in the paraelectric state [19]. Additionally, a pseudo-cubic structure of the PST film may exhibit broad and diffuse modes due to residual scattering from A-site cation inhomogeneity (i.e., composition inhomogeneity in Pb and Sr sites) and/or stress.

The aforementioned anisotropy and sign of stress in the PST film: in-plane (bi-axial) compressive stress and out-of-plane tensile stress can stem from a number of factors: (a) thermal mismatch between PST and Al_2O_3, (b) presence of grains with different orientations in the film, (c) presence of oxygen vacancies, (d) lattice mismatch

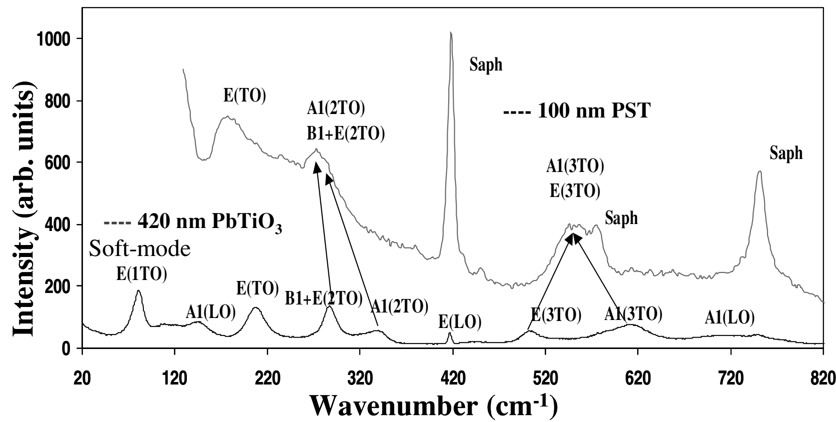

Figure 11 Raman spectra of 100 nm $(Pb_{0.3}Sr_{0.7})TiO_3$ film on (0001) sapphire and 420 nm $PbTiO_3$ film.

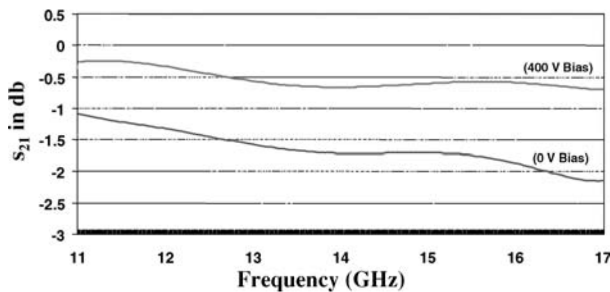

Figure 12 Insertion loss versus frequency for PST film at zero bias and 400 V bias between the center conductor and the ground lines.

between (111) PST and (0001) sapphire, and (e) A-site cation inhomogeneity. In the PST/sapphire heterostructure, considering the small difference between thermal coefficient of $SrTiO_3$ ($\alpha_{SrTiO_3} = 10 \times 10^{-6}$/K) and sapphire ($\alpha_{Al_2O_3} = 8.8 \times 10^{-6}$/K), a thermal mismatch contribution to stress may be neglected. The observation of epi-PST films eliminates the contribution of stress from grains with different orientations. However, due to the high deposition rates (10–15 nm/min) and as-deposited (and unannealed) condition of the PST film, oxygen vacancies may substantially contribute to this complex stress pattern [10]. Please note that the deposition conditions (such as oxygen partial pressure and deposition temperature) are yet to be optimized. Moreover, the effect of stress-inducing threading dislocations and composition inhomogeneity, as reflected in Figs 7 and 11, may also manifest as a source of stress.

3.3. High frequency (7 to 17 GHz) data

Fig. 12 shows the measured insertion loss (magnitude of S_{21}) for 0 V bias and 400 V bias between the center conductor and the ground lines. The insertion loss at zero bias is between 1 dB at 11 GHz and 2.2 dB at 17 GHz, whereas the insertion loss at 400 V bias improved to 0.25 dB at 11 GHz and 0.7 dB at 17 GHz. The improvement in insertion loss is an indication of tunability with applied dc bias, and the low insertion loss is also an indication of the relatively low tan δ in the PST film.

The phase shift of the PST film is illustrated in Fig. 13. It shows the swept frequency measurement of the phase of S_{21} in degrees for 0 V bias and 400 V bias (40 kVcm^{-1}) between the center conductor and the ground lines. The calculated ε_r at 12 GHz for the PST film is 200 (at zero bias) and 140 (at 400 V bias); i.e., a tunability of approximately 30%. The loss-tangent of the film at 12 GHz was estimated to be ~0.05 and 0.03 at 400 V bias. The material FOM and device FOM (or K-factor) were determined to be 632 and approximately 13 degrees/dB, respectively.

Fig. 14 shows the calculated dielectric loss in the PST thin film at zero bias and 400 V bias. As one may observe, the dielectric loss contribution due to the film is greatly reduced at 400 V; this due to the large tunability in both the ε_r and tan δ.

3.4. Microwave property-nanostructure-composition-stress relationships

Numerous past studies have shown that magnitude of ε_r in ferroelectric thin films, when compared to single crystals and/or bulk polycrystalline materials of the same composition, is significantly lower due to the effects of elastic and electrical boundary conditions [20], interfacial layer [21–24], and/or Schottky barriers at the film-electrode interfaces [25, 26]. The effects of elastic stress on the diminution of ε_r have been explained using a phenomenological approach [27–31]. In comparison to the ε_r (>10000) of bulk PST [9], the current study of epi-PST film on sapphire and in CPW structure gives a zero-bias ε_r of 200; a result that is consistent with the results of biaxially stressed $SrTiO_3$, where the permittivity was also significantly lower [32, 33]. As noted in the discussions of the observed nanostructure in Section 3.2, in-plane compressive stress is probably the primary factor for the low in-plane ε_r of epi-PST film. However, due to the non-uniform field distribution in a CPW structure, it may be

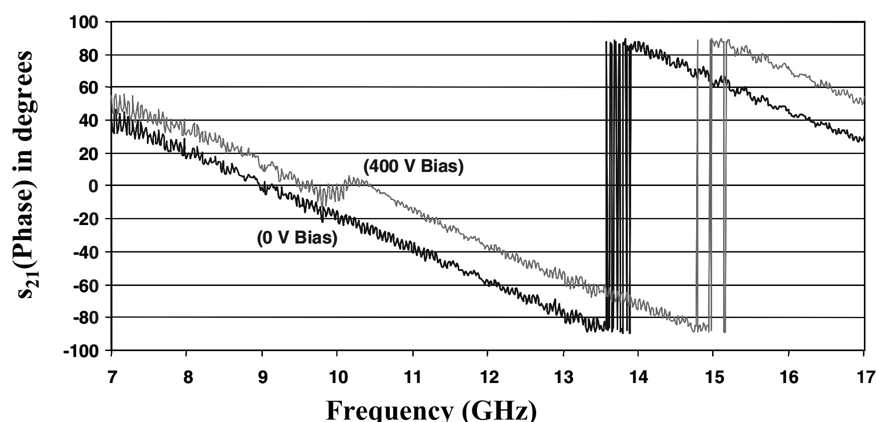

Figure 13 Comparison of the phase of S_{21} for PST film at zero bias and 400 V bias between the center conductor and the ground lines.

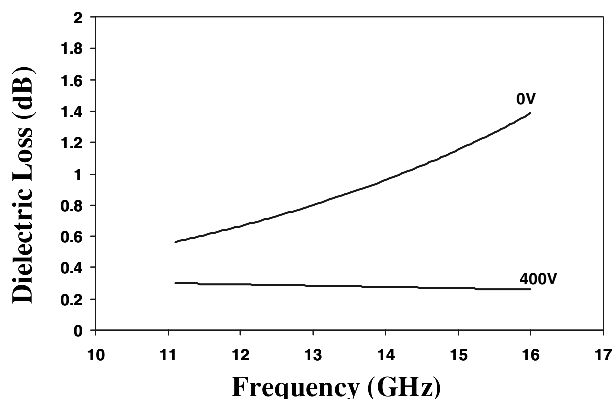

Figure 14 Frequency dependence of the dielectric loss contribution due to the PST thin film at zero bias and 400 V bias.

difficult to quantitatively address the influence of stress on ε_r and tunability.

In general, dielectric loss stems from intrinsic losses [34–36] due to multiple-phonon absorption (single crystal), losses related to charged defects (one-phonon absorption and phonon scattering), relaxation losses and losses due to domain walls [37–39]. Although, in this current study on PST films, it was intended to minimize the domain wall contribution to tan δ by controlling the $Pb_xSr_{(1-x)}TiO_3$ composition (i.e., $x = 0.3$), the potential existence of micro domains from composition inhomogeneity and/or stress are sources of loss. Additionally, stress-inducing threading dislocations, which are charged defects [40], could introduce one-phonon absorption and phonon scattering. However, the anisotropy and sign of stress in the PST film (discussed in Section 3.2) must be the predominant factor for extrinsic dielectric loss. Indeed, a previous study [10] has correlated the extrinsic dielectric loss with oxygen vacancy-mediated tetragonal distortion, D (D = ratio of the in-plane to out-of-plane lattice parameter), in BST films. At microwave frequencies (1–20 GHz), BST films with D = 1 exhibited the highest material FOM. From the aforementioned discussions, one may infer that a combination of different factors lead to the observed tan δ. The presence of charged and stress inducing threading dislocations, oxygen vacancies, lattice mismatches between PST and sapphire, and A-site composition inhomogeneity contribute to tan δ of epi-PST film.

3.5. Selection of composition, substrate, and process parameters

The current discussions on processing, nanostructure, and microwave properties of epi-PST thin films provide a rational basis for the selection of PST composition, substrate, and process parameters for the fabrication of optimized CPW phase shifters with very high figure of merit and operable at room temperature.

The composition of $Pb_xSr_{(1-x)}TiO_3$ must be in the Curie–Weiss range (i.e., $x < 0.3$) to minimize the domain wall contribution to dielectric loss, while maintaining the high tunability. The use of MOCVD in conjunction with the advanced DLI system (with its accurate control of the flow rates of individual cation precursors) can make this approach feasible.

To minimize the in-plane, biaxial stress and to achieve a tetragonal distortion (D) of unity in PST films, cubic substrates with close lattice match to PST or suitable buffer layers on substrates may be more appropriate. For example, Jia *et al.* [41] have studied the microwave properties of pulsed laser deposited $SrTiO_3$ on homoepitaxial buffer layers (2–25 nm) of $LaAlO_3$ on single crystal $LaAlO_3$ substrate. Cross-sectional TEM showed that the buffer layers had many defects, but aided in reducing the stress so that high quality and stress-free $SrTiO_3$ grew epitaxially. It was also found that the quality factor of the microwave device was improved by more than 50%. A similar approach may be implemented with the PST/sapphire system, by using thin buffer layers of crystalline oxides to achieve epitaxial cube-on-cube growth, as well as to minimize stress and

stress-induced charged defects (threading dislocations) in the over layer of PST.

To ascertain the deposition of epi-PST films in this study, the MOCVD growth was carried out in the mass-transport controlled region, but at very high deposition rate. Given a small thermal and lattice mismatch with an appropriate substrate or buffered surface on sapphire, a high temperature (>500°C) and low deposition rate (<5 nm/min) will aid in the deposition of very high quality of epi-PST films with phase purity because of the ease of ad-atom migration to equilibrium positions. However, the control of oxygen stoichiometry and A-site composition homogeneity, to achieve defect-free and stress-free epi-PST films having D = 1, must be achieved through designed CVD experiments, coupled with doping and appropriate post annealing treatments in oxygen [42].

4. Summary

Voltage tunable $Pb_{0.3}Sr_{0.7}TiO_3$ (PST) thin films (90–150 nm) on (0001) sapphire were deposited by metal-organic chemical vapor deposition at rates of 10–15 nm/min. The as-deposited epitaxial PST films were characterized by RBS, X-ray methods, FESEM, HRTEM, Raman spectroscopy, and electrical methods (7–17 GHz) using coplanar waveguide test structures. The epitaxial relationships were as follows: out-of-plane alignment of [111] PST//[0001] sapphire, and orthogonal in-plane alignments of $[1\bar{1}0]$ PST//$[10\bar{1}0]$ sapphire and $[\bar{1}\bar{1}2]$ PST//$[1\bar{2}10]$ sapphire. The microwave properties, characterized using CPW transmission lines and resonators, indicated that the insertion loss at zero bias is between 1 dB at 11 GHz and 2.2 dB at 17 GHz, whereas the insertion loss at 400 V bias improved to 0.25 dB at 11 GHz and 0.7 dB at 17 GHz. The calculated ε_r at 12 GHz is 200 (at zero bias) and 140 (at 400 V bias); i.e., a tunability of approximately 30%. The loss-tangent of the film at 12 GHz was estimated to be ~0.05 and 0.03 at 400 V bias. The in-plane compressive stress is probably the primary factor for the low in-plane ε_r of epi-PST film, and the presence of charged and stress inducing threading dislocations, oxygen vacancies, in-plane (bi-axial) compressive stress and out-of-plane tensile stress, and A-site composition inhomogeneity in PST contribute to tan δ. It is noted that the material FOM and device FOM (or K-factor) were determined to be 632 and approximately 13 degrees/dB, respectively.

The guidelines for selection of PST composition, substrate, and process parameters for the fabrication of optimized CPW phase shifters with very high FOM and operable at room temperature are as follows: (1) a PST composition with $x<0.3$, (2) the use of cubic substrates with close lattice match to PST or suitable buffer layers on sapphire substrates, and (3) MOCVD of PST at low deposition rate (<5 nm/min), coupled with doping and appropriate post annealing treatments in oxygen.

Acknowledgements

SKD would like to acknowledge support of Dr Deborah Van Vechten of the Office of Naval Research, Dr. Stuart A. Wolf of the Defense Science Office at Defense Advanced Research Projects Agency (DARPA), and the Frequency Agile Materials for Electronics (FAME) program at DARPA (contract number N00014-00-1-0471).

References

1. M. J. DALBERTH, R. E. STAUBER J. C. PRICE, C. T. ROGERS, and D. GALT, *Appl. Phys. Lett.* **72** (1998) 507.
2. H.-D. WU and F. S. BARNES, *Integr. Ferroelectr.* **22** (1998) 291.
3. D. S. KORN and H.-D. WU, *ibid.* **24** (1999) 215.
4. G. SUBRAMANYAM, F. W. VAN KEULS, and F. A. MIRANDA, *IEEE Microwave Guided Wave Lett.* **8** (1998) 78.
5. F. W. VAN KEULS, R.R. ROMANOFSKY, D. Y. BOHMAN, M. D. WINTERS, F. A. MIRANDA, C. H. MUELLER, R. E. TREECE, T. V. RIVKIN, and D. GALT, *Appl. Phys. Lett.* **71** (1997) 3075.
6. S. S. GEVORGIAN, D. I. KAPARKOV and O. G. VENDIK, *IEEE Proc. Microwave, Antennas and Propagation* **141** (1994) 501.
7. A. T. FINDIKOGLU, Q. X. JIA, X. D. WU, G. J. CHEN, T. VENKATESAN and D. W. REAGOR, *Appl. Phys. Lett.* **68** (1996) 1651.
8. W. WILBUR *et al.*, *Integr. Ferroelectr.* **19** (1998) 149.
9. Y. SOMIYA, A. S. BHALLA and L. E. CROSS, *Int. J. of Inorg. Mater.* **3** (2001) 709.
10. W. J. KIM, W. CHANG, S. B. QADRI, J. M. POND, S. W. KIRCHOEFER, D. B. CHRISEY and J. S. HORWITZ, *Appl. Phys. Lett.* **76** (2000) 1185.
11. R. A. YORK, A. S. NAGRA, P. PERIASWAMY, O. AUCIELLO, S. K. STREIFFER and J. IM, *Integr. Ferroelectr.* **34** (2001) 177.
12. E. CARLSSON and S. GEVORGIAN, *IEEE T. Micro. Theory* **47** (1999) 1544.
13. S. GEVORGIAN, T. MARTINSSON, A. DELENIV, E. KOLLBERG and I. VENDIK, *IEEE Proc. Microwave, Antennas and Propagation* **144** (1997) 145.
14. S. NOMURA and S. SAVADA, *J. Phys. Soc. Jpn.* **10** (1955) 108.
15. W. J. KIM, H. D. WU, W. CHANG, S. B. QADRI, J. M. POND, S. W. KIRCHOEFER, D. B. CHRISEY and J. S. HORWITZ, *J. Appl. Phys.* **88** (2000) 5448.
16. K. WASA and S. HAYAKAWA, in "Handbook of Sputter Deposition Technology" (Noyes Publications, Park Ridge, New Jersey, 1992) p. 175.
17. T. ZHELEVA, K. JAGANNADHAM and J. NARAYAN, *J. Appl. Phys.* **75** (1994) 860.
18. K. ABE, N. YANASE, K. SANO and T. KAWAKUBO, *Integr. Ferroelectr.* **21** (1998) 197.
19. J. MENG, G. ZOU, Y. MA, X. WANG and M. ZHAO, *J. Phys.-Condens. Mat.* **6** (1994) 6549.
20. O. G. VENDIK and L. T. TER-MARTIROSYAN, *Sov. Phys.-Solid State* **36** (1994) 1778.
21 K. ABE and S. KOMATSU, *Jap. J. Appl. Phys.* **32** (1993) L1157.
22. C. ZHOU and D.M. NEWNS, *J. Appl. Phys.* **82** (1997) 3081.
23. C. BASCERI, S.K. STREIFFER, A.I. KINGON and R. WASER, *J. Appl. Phys.* **82** (1997) 2497.

24. H.C. LI, W. SI, A.D. WEST and X.X. XI, *Appl. Phys. Lett.* **73** (1998) 464.
25. G.W. DIETZ, W. ANTPOHLER, M. KLEE and R. WASER, *J. Appl. Phys.* **78** (1995) 6113.
26. G. W. DIETZ and R. WASER, *Thin Solid Films* **299** (1997) 53.
27. S. STREIFFER, C. BASCERI, C.B. PARKER, S.E. LASH, and A.I. KINGON, *J. Appl. Phys.* **86** (1999) 4565.
28. N. A. PERTSEV, A. G. ZEMBILGOTOV and A. K. TAGANTSEV, *Phys. Rev. Lett.* **80** (1998) 1988.
29. N. A. PERTSEV, A. G. ZEMBILGOTOV, S. HOFFMANN, R. WASER and A.K. TAGANTSEV, *J. Appl. Phys.* **85** (1999) 1698.
30. N. A. PERTSEV, A. K. TAGANTSEV and N. SETTER, *Phys. Rev. B* **61** (2000) R825.
31. B. DESU, V. P. DUDKEVICH, P. V. DUDKEVICH, I. N. ZAKHARCHENKO and G.L. KUSHLYAN, *MRS Symp. Proc.* **401** (1996) 195.
32. E. HEGENBARTH and C. FRENZEL, *Cryogenics* **7** (1967) 331.
33. T. M. SHAW, Z. SUO, M. HUANG, E. LINIGER, R. B. LAIBOWITZ and J. D. BANIECKI, *Appl. Phys. Lett.* **75** (1999) 2129.
34. V. L. GUREVICH and A. TAGANTSEV, *Adv. Phys.* **40** (1991) 719.
35. A. K. TAGANTSEV, in “Ferroelectric Ceramics: Tutorial Reviews, Theory, Processing, and Applications,” edited by N. Setter and E. L. Colla (Springer-Verlag, New York, LLC, 1992) p. 127.
36. O. VENDIK, L. TER-MARTIROSYAN and S. ZUBKO, *J. Appl. Phys.* **84** (1998) 993.
37. J. O. GENTNER, P. GERTHSEN, N. A. SCHMIDT and R.E. SEND, *ibid.*. **49** (1978) 4595.
38. K.H. HÄRDTL, *Ceram. Int.* **8** (1982) 121.
39. G. ARLT, U. BOTTGER, and S. WITTE, *Appl. Phys. Lett.* **63** (1993) 602.
40. S. MAHAJAN, *Prog. Mater. Sci.* **42** (1997) 341.
41. Q. X. JIA, A.T. FINDIKOGLU, D. REAGOR and P. Lu, *Appl. Phys. Lett.* **73** (1998) 897.
42. C. K. BARLINGAY and S. K. DEY, *Thin Solid Films*, **272** (1996) 112.